Adaptive Hybrid Filtering & Damping Control for Grid-Following MMC

Pengxiang Huang and Luigi Vanfretti
Depart. Electrical, Computer, and Systems Engineering
Rensselaer Polytechnic Institute
Troy, NY, 12180, U.S.A
huangp2@rpi.edu, vanfrl@rpi.edu

***Abstract*—Oscillation events between grid-following MMC (GFL-MMC) and ac systems in the medium-/high-frequency (MF/HF) range have been widely reported in recent years. To address this issue, this paper proposes an adaptive hybrid filtering and damping (AHFD) control design method to address oscillation issues within the MF/HF range. When lowpass filters with proposed designs are placed into control loops, the negative damping region in the HF range of MMC is eliminated, effectively limiting the potential oscillations to the MF range. In addition, based on online resonance detection, an active narrowband damper is automatically configured to add and adjust positive damping to MMC at the system resonance frequency in the MF range. Both the damper gain and damping range of this narrowband damper are autonomously adjusted through an adaptive tuning unit, thereby eliminating the need for prior knowledge of the MMC's physical characteristics (i.e., its model parameters) for damper design and tuning. Electromagnetic Transient (EMT) simulation results validate the efficacy of the proposed AHFD control method in a power system involving GFL-MMC and long overhead transmission.**

***Index Terms*—modular multilevel converter (MMC), high-frequency resonance, medium-frequency resonance, oscillation, adaptive control**

I. Introduction

GRID-following modular multilevel converters (GFL-MMCs) are known to develop wideband oscillations with the ac system they connect to in medium-frequency (MF) (200 Hz to $\sim$1 kHz) and high-frequency ($>$ $\sim$1 kHz) range [1]. Several oscillation events within these frequency ranges have been reported in the literature, including: an oscillation around 1.7 kHz in the INELFE link [2]; a 1270 Hz oscillation at the Lu'xi MMC station [3]; consecutive oscillations at 1810 Hz and 695 Hz in the Yu'e MMC project [4]; and a 1550 Hz oscillation in the Zhangbei MMC project [5].

The rootcause of these MF/HF oscillations is attributed to the system resonance frequency falling into the delay-induced negative damping region of the MMC. To mitigate such oscillations, several methods have been extensively studied in the literature. Among the different methods proposed, active methods are particularly attractive because they avoid the cost of power loss and do not require additional installation space compared to passive methods [6] (especially for offshore applications). Active methods to suppress MF/HF oscillations include wideband filtering [2]–[5] and narrowband damping [7]–[9]. The former method involves the integration of lowpass filters (LPFs) into existing control loops, which is effective in eliminating the negative damping of the MMC impedance in the frequency range defined by the stopband of LPFs. Nevertheless, the phase shift within the LPFs' transition band and passband will increase the negative damping of MMC in the MF region, especially when coupled with phase lags posed by time delay effects, thereby exacerbating stability issues of MMC at MFs. Most of the existing literature focuses on optimizing LPFs' designs to avoid including potential resonance frequencies in the negative damping range of MMC after applying LPFs. However, the efficacy varies widely from case to case, as a pre-design cannot accommodate all possible resonance conditions in the MF range. In addition, the literature does not provide a clear explanation of how to design LPFs without compromising the stability of control loops. On the other hand, narrowband damping uses a feedforward damping function along with a bandpass filter (BPF) that can selectively and narrowly add positive damping to the MMC impedance around the system resonance frequency. However, its damping performance is impacted by delay-induced phase lag, and such phase lag is difficult to compensate for over a wide range of frequencies. Additionally, the grid-voltage feed-forward (GVF) loop significantly changes the magnitude of the MMC impedance at MFs and HFs, making narrowband damping design more challenging. Therefore, narrowband damping can be effective when placing an LPF with a relatively small cutoff frequency in the GVF loop, as suggested by [1], [8]. There is, however, a possibility that the LPF could impair the MMC's fault ride-through capability if heavy filtering is applied to the GVF loop.

In addressing the challenges of the wideband filtering and narrowband damping methods mentioned above, this work introduces an adaptive hybrid filtering-damping (AHFD) control strategy designed to suppress MF/HF oscillations of a GFL-MMC. By inserting specifically designed LPFs into the current feedback and GVF loops, the endpoint of the negative damping region is pushed closer to the boundary frequency between the MF and HF range. Subsequently, an adaptive narrowband damper is programmed, allowing for selectively adding and self-adjusting the positive damping at any identified resonance frequency within the negative damping range. Both the damping gain and the damping range are automatically adjusted through an adaptive tuning unit introduced in this paper. The

contributions of this paper can be summarized as follows:

1) Develop a hybrid approach to damp MF/HF oscillations between GFL-MMC and ac systems by using LPFs and narrowband damper
2) Provide a systematic method for designing LPFs with a consideration of control loop stability and control's effect on MMC impedance shape
3) Propose an adaptive tuning method for the damping gain and damping width of the narrowband damper

The rest of this paper is organized as follows: Section II describes the system under study and describes how impedance models characterize the stability issues that arise between the MMC and the ac system within the MF/HF range. Sections III and IV illustrate the effect of lowpass filters and narrowband damper on the MMC impedance, along with their respective systematic design considerations and procedures. EMT simulations to illustrate the effectiveness of the proposed AHFD control are shown in Section V. Section VI concludes the work.

II. System Under Study and Impedance Characteristic

A. System Description

Fig. 1 presents the circuit and control diagram of a GFL-MMC with the proposed AHFD method, where the ac grid to which the MMC connects is modeled as an ideal voltage source behind a line impedance Z_{line}. The MMC pole control typically employs one of three modes: 1) dc voltage control with a unity power factor (i.e., $I_s^{q*}=0$); 2) active power and reactive power control; or 3) dc voltage control with reactive power regulation. In all three modes, controllers (marked as $G_v(s)$, $G_P(s)$ and $G_Q(s)$) are nested with an inner ac current control loop (denoted as $G_c(s)$), which is used to control i_d and i_q to follow the command value generated by the outer control loops. Valve control incorporates second-order circulating current suppressing control (CCSC) [10] and a direct modulation scheme with nearest-level control (NLC) [11]. The parameters of the GFL-MMC studied are summarized in Table I.

The proposed AHFD control consists of two parts: 1) lowpass filtering in the GVF loop and the inner ac current control loop, carried out by $H_{fv}(s)$ and $H_{fi}(s)$, respectively (shown in blue in Fig. 1); and 2) adaptive narrowband damping via an additional ac voltage feedforward loop, accomplished using an online resonance detection unit (shown in green in Fig.1) and damping controller $H_d(s)$ (shown in red in Fig.1). As depicted in Fig. 1, the AHFD control loop operates independently from the outer control loops, indicating its applicability to GFL-MMCs across different control modes. However, to limit the scope of the paper, in the sequel, a dc-bus voltage-controlled MMC with a unity power factor (labeled as the "$V_{dc}\&Q=0$" mode) is considered.

B. Models and Characteristics of the MMC-Grid System

1) Impedance of MMC and Grid:

As noted in [12], [13], the internal dynamics of the MMC and CCSC only affect the low-frequency impedance of the MMC. In addition, the influence of the phase-locked loop (PLL) diminishes above 200 Hz, a phenomenon attributed to the inherent second-order filtering function of the PLL control structure [1], [6]. Furthermore, the effect of the dc-bus voltage control effect is attenuated by the arm inductance and the submodule's (SM) capacitance in the MF/HF range [1]. As a result, the simplified control block diagram of the MMC operating in the "$V_{dc}\&Q=0$" mode can be represented as shown in Fig. 2, where $G_c(s)$ is the transfer function representing the current control effect, and "R_0+sL_0" symbolizes the half-arm impedance of the MMC. Using Mason's gain formula, the ac current i_s can be calculated as follows:

$$i_s=\frac{G_c(s)e^{-sT_d}}{sL_0+R_0+G_c(s)e^{-sT_d}}i_{ref}+\frac{1-e^{-sT_d}}{sL_0+R_0+G_c(s)e^{-sT_d}}v_s. \tag{1}$$

Based on (1), the impedance model of MMC can thus be

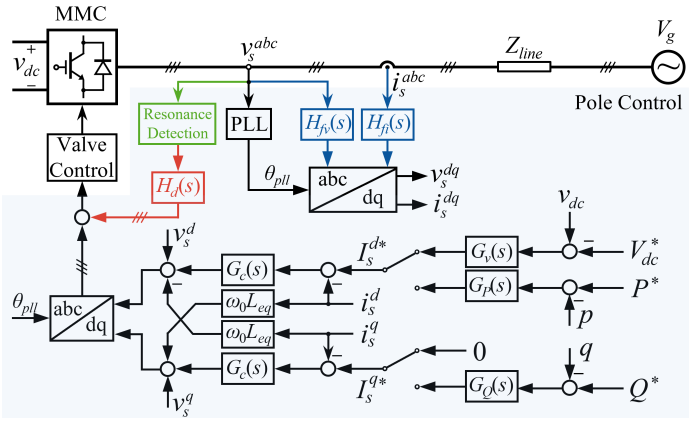

Fig. 1. A single-line diagram of a GFL-MMC with AHFD control.

TABLE I
Electrical Parameters of the MMC and AC System

Parameter	Symbol	Value	Unit
rated active power	P_N	900	MW
ac-side voltage	U_N	300	kV rms ph-ph
dc-side voltage	V_{dc}	± 320	kV
arm impedance	R_s+jL_s	$0.1+j0.05$	Ω
# of SM per arm	N_{sm}	50	-
SM capacitance	C_{sm}	1.2	mF
time delay	e^{-sT_d}	350	μs
π-section impedance	R_0+jL_0	$(29.8+j1.58)\times 10^{-3}$	Ω /mile
π-section capacitance	jC_0	$j17.9\times 10^{-9}$	F/mile

TABLE II
MMC Control Specifications

Control functions	K_p	K_i	K_d
dc voltage control	0.0065	0.2	NA
ac current control	22.2	27915.5	7.85
CCSC	22.2	13957.7	31.42
phase-locked loop	1.48×10^{-4}	0.0093	N/A

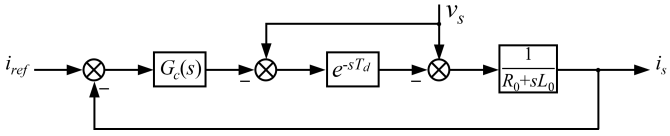

Fig. 2. Simpliefied block diagrams of MMC with grid voltage feedforward.

described by a simple transfer function:

$$Z_{MMC}(s) = \frac{v_s}{i_s} = \frac{sL_0 + R_0 + G_c(s)e^{-sT_d}}{1 - e^{-sT_d}} = \frac{N_{MMC}(s)}{D_{MMC}(s)} \quad (2)$$

where $G_c(s) = H_i(s - j\omega_1) - jK_d$, $H_i(s)$ is the PI compesator of ac current controller and K_d is the decoupling gain. The simplified impedance model derived from the block diagram, using Mason's gain formula, aligns with the results detailed in [1]. Given this agreement and due to space limit, the validation of impedance model through numerical scan is omitted in this paper.

In this work, a long overhead transmission line (OTL) and an ac voltage source are utilized to represent a very weak ac grid. To accurately characterize the MF/HF characteristics of a long OTL, multiple cascaded sections π are used to model Z_{line} [14].

2) Wideband Stability Enhancement by AHFD:

Fig. 3 compares the MMC impedance (Z_{MMC}) with the impedance of a 100-mile OTL (Z_{line}) modeled by 10 cascaded π-sections. The parameters for MMC and OTL are shown in Table I and II, respectively. From the comparison in Fig. 3, it can be observed that $Z_{MMC}(s)$ forms three series resonances with $Z_{line}(s)$ at 1564, 2387, and 4633 Hz. At each of these intersection points, the phase difference exceeds 180°, indicating three unstable oscillations between the MMC and the OTL. The oscillation at 2387 Hz is predicted to be dominant because of the largest phase difference among the three.

In Section I, the limitations of existing methods in damping these HF oscillations have been noted, and the AHFD control method is proposed to overcome them. This approach consists of two steps:

Step 1: Insert LPFs into both the GVF and ac current control loop to eliminate the negative damping of the MMC above approximately 1000 Hz, referred to as the HF range. As a result, oscillation events above $\sim$ 1000 Hz can be avoided.

Step 2: Introduce a narrowband damper, which is self-adjusted, to enhance the passivity of the MMC impedance around the resonance frequency between the MMC and the ac grid at MF. As a consequence, the associated oscillation in the MF range can be damped.

As indicated in the first step, the purpose of using LPFs is to limit the negative damping region to the MF range only, rather than to remove as much of it as possible from the MMC impedance above 200 Hz. In this step, multiple MF/HF oscillation issues are converted into a single MF oscillation

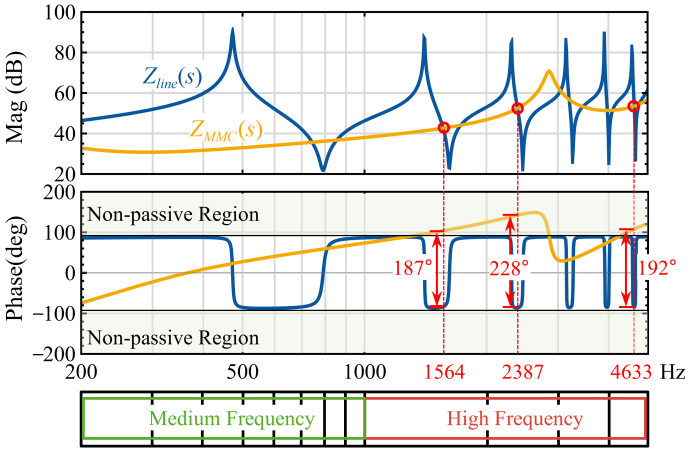

Fig. 3. Impedance responses of GFL-MMC defined by (2), in comparison with OTL impedance modeled by 10 π-sections.

issue, making the narrowband damper work in the MF range more targeted and effective.

Fig. 4 shows the block diagram of the MMC incorporating the proposed AHFD control. The following sections will explore the detailed considerations for the design of $H_{fv}(s)$, $H_{fi}(s)$, and $H_d(s)$.

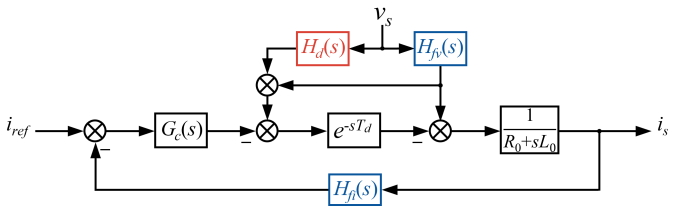

Fig. 4. Block diagram of MMC with hybrid filtering and damping control.

III. Lowpass Filtering

The LPFs are integrated at both the GVF and current feedback loops, see Fig. 1 and 4. The filtering function applied in this study utilizes the following second-order lowpass filters:

$$H_{fi}(s) = \frac{(2\pi f_{ni})^2}{s^2 + Q^{-1}(2\pi f_{ni})s + (2\pi f_{ni})^2} \quad (3)$$

$$H_{fv}(s) = \frac{(2\pi f_{nv})^2}{s^2 + Q^{-1}(2\pi f_{nv})s + (2\pi f_{nv})^2} \quad (4)$$

where f_{ni} and f_{nv} are the cutoff frequencies of the LPFs in the ac current feedback loop and the GVF loop, respectively. Q is the quality factor, which is generally selected to be $\sqrt{2}/2$ to provide an approximately constant gain below the cutoff frequency.

The lowpass filtering effect on the MMC impedance model can be reflected by multiplying $H_{fi}(s)$ with $G_c(s)$ and multiplying $H_{fv}(s)$ with e^{-sT_d}, which yields

$$Z^f_{MMC}(s) = \frac{N^f_{MMC}(s)}{D^f_{MMC}(s)} = \frac{sL_0 + R_0 + H_{fi}(s)e^{-sT_d}G_c(s)}{1 - H_{fv}(s)e^{-sT_d}} \quad (5)$$

where the superscript f denotes the lowpass filtering effect.

A. Design considerations of $H_{fi}(s)$

As indicated in Fig. 4, $H_{fi}(s)$ is effectively connected in series with $G_c(s)$, thereby $H_{fi}(s)$ may affect the phase margin of the current control loop gain, which is $e^{-sT_d}H_i(s)/(sL)$. Therefore, it is crucial to ensure that the phase shift introduced by $H_{fi}(s)$ does not lead to instability of the loop gain. Letting the bandwidth of the loop gain be f_{cb}, the phase shift generated by $H_{fi}(s)$ at f_{cb} can be calculated by:

$$\theta_{fi}(f)\,|_{f=f_{cb}} = \tan^{-1}\left(\frac{f_{ni}\cdot f_{cb}}{Q\cdot[(f_{ni})^2-(f_{cb})^2]}\right). \tag{6}$$

Theoretically, with the LPF included in ac current control loop, even if the resulting phase margin of the loop gain is 1°, it shall be sufficient to maintain the stability of current control loop. Yet, for practical purposes and increased safety, it is advisable to maintain a worst-case phase margin at about 30°. As a result, the minimum cutoff frequency of the LPF in the current feedback loop can be calculated as follows:

$$\tan^{-1}\left(\frac{f_{ni}\cdot f_{cb}}{Q\cdot[(f_{ni})^2-(f_{cb})^2]}\right) \geq \phi_m - 30^\circ \tag{7}$$

where f_{cb} and ϕ_m are the pre-designed bandwidth and phase margin of the loop gain (i.e., $e^{-sT_d}G_i(s)/(sL)$), respectively. For instance, if the ac current control is designed to provide a bandwidth of 300 Hz and a phase margin of 60° before applying the filter, the chosen cutoff frequency f_{ni} should not be less than 841 Hz. It is worth pointing out that the design of $H_{fi}(s)$ presumes that the ac current control is already designed based on desired current dynamics. Therefore, when ϕ_m is already less than 30°, $H_{fi}(s)$ should be disabled, or the current controller should be redesigned to provide a larger ϕ_m at f_{cb}.

B. Design considerations of $H_{fv}(s)$

To understand how $H_{fv}(s)$ affects the MMC impedance, Fig. 5 plots the frequency responses of $1/D^f_{MMC}(s)$ with different selection of f_{nv}. For comparison, the response of $1/D_{MMC}(s)$ is also included. Without the filter, $1/D_{MMC}(s)$ leads to a phase boost in the MMC impedance in the frequency ranges (200 Hz, $0.5/T_d$ Hz) and ($1/T_d$ Hz, $1.5/T_d$ Hz), labeled as Region 1 and 3 in Fig. 5, respectively. It also causes a phase reduction in the ranges ($0.5/T_d$ Hz, $1/T_d$ Hz) and ($1.5/T_d$ Hz, 5000 Hz), denoted as Region 2 and 4 in Fig. 5. Considering that the MMC impedance exhibits an inductive phase characteristic in the frequency range above the ac current control bandwidth, the two phase-reduction regions will enhance the passivity of MMC, which is advantageous for stability of MMC. The phase boost regions, on the other hand, increase the phase response of MMC impedance, thereby jeopardizing its passivity. Moreover, as can be seen from the magnitude response plotted in Fig. 5, $1/D_{MMC}(s)$ introduces a significant resonant peak to the impedance shape of the MMC, making it more prone to interaction with the connected ac system.

Fig. 5 also illustrates that reducing f_{nv} attenuates the influence of $1/D^f_{MMC}(s)$ on both the magnitude and the phase response of the MMC in the HF range, and this effect becomes increasingly noticeable as f_{nv} decreases. Nonetheless, setting a f_{nv} too low should be avoided, as it may significantly curtail the feedforward gain, thereby undermining the transient performance of the GVF. Furthermore, a smaller f_{nv} causes the phase of $1/D^f_{MMC}(s)$ to become positive at a lower frequencies, effectively shifting the starting frequency of Region 2 towards a lower frequency range. Given that the purpose of lowpass filtering is to move the negative damping region of MMC into the MF range, the selection of f_{nv} must ensure that the lower end of Region 2 is less than the upper end of $N^f_{MMC}(s)$'s negative damping region nearby the MF region. Therefore, f_{nv} can be computed by numerically solving the following equations:

$$\begin{cases} N^f_{MMC}(j2\pi f) = 0 \\ N^f_{MMC}(j2\pi f^-) > 0 \;\&\; N^f_{MMC}(j2\pi f^+ < 0)) \\ \angle 1/D^f_{MMC}(j2\pi f) \geq 0^\circ \end{cases} \tag{8}$$

C. Impedance Characteristic of MMC with LPFs

To elucidate the effects of $H_{fi}(s)$ and $H_{fv}(s)$ on the MMC impedance, we incorporate the LPFs with the proposed filter designs into the MMC whose parameters are early provided in Table I and II. For the current feedback loop, $H_{fi}(s)$ with

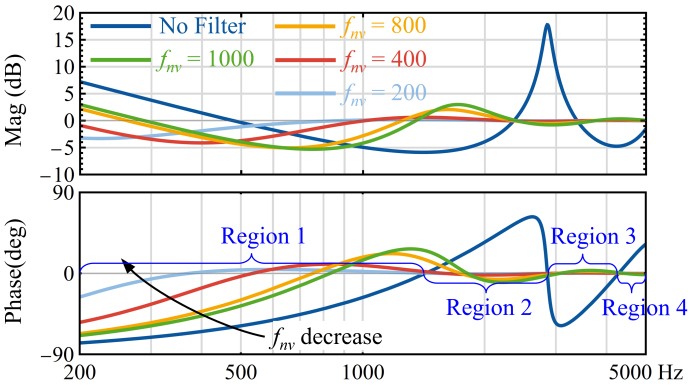

Fig. 5. Frequency responses of $1/D^f_{MMC}(s)$ with different f_{nv}. Parameters of MMC are from Table I and II.

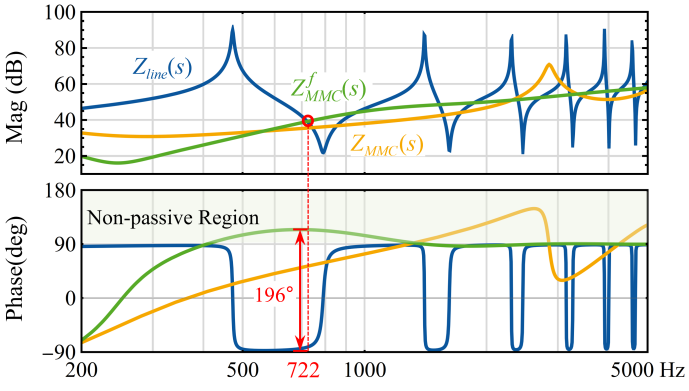

Fig. 6. Impedance responses of the MMC without lowpass filters (orange), with lowpass filters (green) and the 100-mile OTL (blue).

$f_{ni} = 1092$ Hz is chosen according to (7), and for the GVF loop, $H_{fv}(s)$ with $f_{nv} = 400$ Hz is selected based on (8). The quality factor of both lowpass filters is set to $\sqrt{2}/2$. Fig. 6 illustrates the resulting MMC impedance (including the filter) and compares it with the OTL impedance that was shown previously in Fig. 3.

The impact of lowpass filtering can be interpreted in several ways. First, the negative damping of MMC above approximately 1400 Hz is eliminated, and the phase response is sustained at about 90°. As a result, while the magnitude intersections between the MMC and OTL cannot be avoided in the HF range, their phase difference is guaranteed to remain below 180°, indicating that no HF oscillation issues should arise. Second, the phase response of MMC between 200 Hz and 1400 Hz is enlarged. This enlarged phase response creates a 196° phase difference between MMC and OTL at the magnitude intersection at 722 Hz, signifying an unstable MF oscillation.

IV. Adaptive Narrowband Damping

A. Fixed-Damping Gain Design Issues

Narrowband damping combines the damping gain, denoted as K_d, with a bandpass filter centered at the resonance frequency f_r, allowing for selectively adding positive damping in a narrow range around f_r. In this work, the narrowband damping control utilizes a complex-coefficient filter (CCF), and the damping function $H_d(s)$ (shown in red in Fig. 1) is subsequently defined as follows:

$$H_d(s) = K_d e^{j\theta} H_{ccf}(s) = K_d e^{j\theta} \frac{2\pi f_b}{s - j2\pi f_r + 2\pi f_b} \tag{9}$$

where f_r represents the center frequency of the CCF (denoted as $H_{ccf}(s)$ in (9)), typically equals to the resonance frequency; f_b signifies filter bandwidth and defines the damping range of $H_d(s)$; K_d is the damper gain. The term $e^{j\theta}$ compensates for the phase lag to which the narrowband damper might be subjected, as per [1], [8].

K_d must be properly selected, otherwise it may shift the resonance frequency into the non-passive regions nearby f_r. In [1], [9], K_d is determined according to a design specification that results in a fixed value, ensuring that the magnitude response of the MMC at f_r remains unchanged upon damper employment. This method is hereafter referred to as the "*fixed-gain design*". Note that when the narrowband damper introduces positive damping to f_r, it also influences the MMC impedance in the vicinity of f_r. More precisely, it introduces a certain amount of inductive impedance below f_r and capacitive impedance above f_r. Consequently, it creates a resonant peak and a resonant dip in the magnitude response of the MMC. When the compensation of negative damping is substantial, the narrowband damper can result in a pronounced resonant peak and dip in the magnitude. This peaking and dipping makes the MMC more likely to interact with the ac grid it connects to, thereby increasing the risk for forming a new resonance between damped MMC and the ac grid.

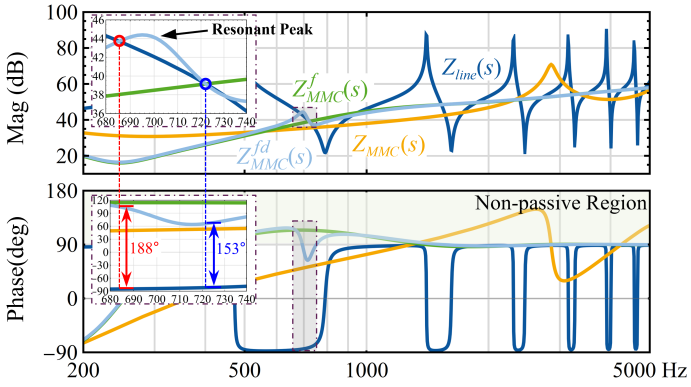

Fig. 7. Impedance responses of the MMC without lowpass filters (orange), with lowpass filters (green), with lowpass filters and narrowband damper (light blue), and the 100-mile OTL (blue)

To show the effect of magnitude peaking and dipping introduced by the narrowband damper, Fig. 7 plots the resulting impedance when the narrowband damper with "*fixed-gain design*" is applied to the "filtered" MMC impedance $Z^{f}_{MMC}(s)$, shown previously in Fig. 6. The superscript fd indicates the lowpass filtering and damping effect. It can be observed in Fig. 7 that, by applying the narrowband damper with "*fixed-gain design*", $Z^{fd}_{MMC}(s)$ has a magnitude equal to $Z^{f}_{MMC}(s)$ at 722 Hz , thus the magnitude of damped MMC and the ac grid still intersect at 722 Hz. Additionally, the phase difference at 722 Hz is reduced to 153°, indicating that there is no oscillation at 722 Hz. However, because the narrowband damper introduces a resonant peak below 722 Hz, an emergent magnitude intersection at 685 Hz exhibits a phase difference of 188°, indicating a new unstable oscillation.

B. Automatic Tuning of Damping Gain and Bandwidth

A solution to the above-mentioned issue could involve expanding the bandwidth of the CCF, f_b, thus enabling the narrowband damper to cover a wider frequency range including the new resonance frequency. However, to choose a proper value for f_b, it is necessary to evaluate the unwanted effects introduced by the damper at the neighboring frequencies of f_r. Since the resonance condition depends on grid configurations, system operating conditions, and MMC control modes, unwanted effects can vary case by case, creating complications for the selection of f_b.

Considering that increasing K_d increases the sharpness of the resonant peak adjacent to f_r, the narrowband damper should be designed to mitigate the oscillation by adding the minimum positive damping possible to MMC, even if the resonance frequency might slightly shift to neighboring frequencies following the application of the damper. Furthermore, the selection of f_b must ensure that the shifted resonance frequency remains within the positive damping range created by the narrowband damper. Therefore, an adaptive method is proposed here to adjust K_d and f_b, in which both parameters are dynamically adjusted according to the intensity of the voltage oscillations around f_r. The implementation of the

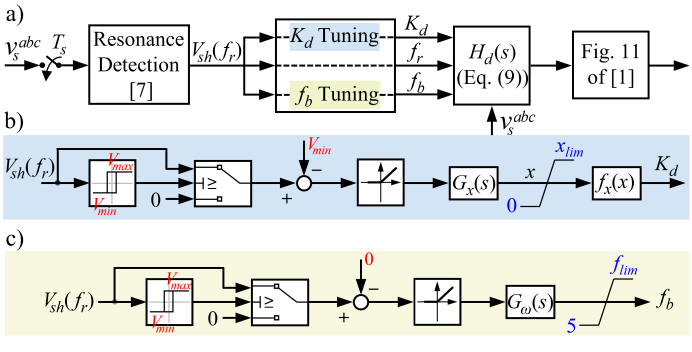

Fig. 8. Control block diagram of the adaptive tuning unit

automatic tuning of K_d and f_b is illustrated in Fig. 8, where the resonance detection block incorporates the interpolated DFT algorithm presented in [15], yielding the amplitude of the voltage oscillation at the identified resonance frequency f_r (denoted as $V_{sh}(f_r)$). Note that in Fig. 8 a), the voltage measurement v_s^{abc} is sampled over a period T_s, indicating that the adaptation of K_d and f_b is updated per T_s.

$V_{sh}(f_r)$ is treated as the input of the adaptive tuning unit determining K_d and f_b, as shown in Fig. 8 b) and c). This input is compared to a preset harmonic limitation, V_{min}, only when its amplitude exceeds V_{max}. The difference between V_{sh} and V_{min} is then fed into a Proportional-Integral (PI) compensator to auto-adjust K_d to a value sufficient for suppressing the oscillation. The PI compensator ceases to function once V_{sh} is reduced below V_{min}, which results in the output of $G_x(s)$ maintaining its level. In addition, the saturation block added to the PI compensator's output ensures its output remains positive but not excessively large to considerably change the MMC impedance around f_r, particularly when the difference between V_{sh} and V_{min} is substantial due to a rapidly growing oscillation. It is noteworthy that the output of $G_x(s)$ is a per-unit (p.u.) value x, which describes the amount of positive conductance, added by the narrowband damper, in terms of a base quantity selected as the conductance of the "filtered" MMC. On the other hand, adaptive regulation of f_b can be achieved in a similar way, as described in Fig. 8 c). The PI compensators $G_x(s)$, $G_\omega(s)$, and the function $f_x(x)$ are defined as follows:

$$G_x(s) = K_{px} + \frac{K_{ix}}{s}; \quad G_\omega(s) = K_{p\omega} + \frac{K_{i\omega}}{s}; \tag{10}$$

$$f(x) = x \frac{\left|\Re\mathfrak{e}\left\{1/Z^f_{MMC}(j2\pi f_r)\right\}\right|}{e^{j\theta}e^{-j2\pi f_r T_d}H_{ccf}(j2\pi f_r)} N^f_{MMC}(j2\pi f_r) \tag{11}$$

C. Design of Adaptive Tuning Unit

1) Design of V_{max}: In the resonance detection block, the identification of f_r requires a comparison between V_{sh} and a preset threshold value A_{th}. The selection of V_{max} should coincide with the amplitude threshold used in the resonance detection block, that is A_{th}.

2) Design of V_{min}: The main objective of the narrowband damper is to mitigate an unstable oscillation at the resonance frequency. However, it may not efficiently suppress the magnitude of the oscillation below the steady-state harmonic or interharmonic levels at the same frequency. Hence, V_{min} should be chosen slightly higher than the background harmonic or interharmonic levels defined by grid code.

3) Design of x_{lim}: The value of x_{lim} can be set to 2, which ensures that the system resonance is effectively damped without causing a change in its frequency. By doing so, after the output of $G_x(s)$ saturates at x_{lim}, further adjustments to the narrowband damper would rely solely on the adaptive tuning of f_b.

4) Design of f_{lim}: As discussed in Section IV.B, the bandwidth of the filter, f_b, should cover the shifted resonance frequency subsequent to the application of the damper. However, assigning an excessively large value to f_b would contradict the main aim of the narrowband damper, which is to limit the damping effect to a narrow range. Therefore, a reasonable choice of f_b could be twice the frequency resolution of the Discrete Fourier Transform (DFT) used in resonance detection block.

V. Simulation Studies

In order to verify the efficacy of the proposed AHFD control method, this section presents numerical simulation results obtained with MATLAB/SIMULINK. The simulation model is constructed based on the system delineated in Fig. 1, where the GFL-MMC operates in "$V_{dc}\&Q = 0$" mode and Z_{line} represents a 100-mile OTL. The key parameters for MMC control and OTL are provided in Tables I and II, respectively.

A. Simulation Setup and Results

The design of the low-pass filters and the adaptive narrowband damper is outlined in Table III, where V_N represents the peak value of PCC voltage between MMC and OTL. The simulation begins with the engagement of two low-pass filters in the MMC controls, while the adaptive narrowband damper is excluded. For demonstration purposes, only a 100 μs time delay attributable to the 10 kHz zero-order hold sampling period of the modulator—is initially included. A further 300 μs time delay is added to the MMC at t = 1 second. As already studied in Section III.C, a 722 Hz growing oscillation can be predicted following the introduction of a 300 μs time delay in the MMC (note that the MMC already has low-pass filters in place).

TABLE III
DESIGN OF ADAPTIVE HYBRID FILTERING & DAMPING CONTROLLER

Parameter	Symbol	Value
quality factor of LPF	Q	1.414
cutoff frequency of $H_{fi}(s)$	f_{ni}	1092 Hz
cutoff frequency of $H_{fv}(s)$	f_{nv}	400 Hz
relay switch-on point	V_{max}	5% V_g
relay switch-off point	V_{min}	2% V_g
saturation value of x	x_{lim}	4
saturation value of f_b	f_{lim}	200 Hz

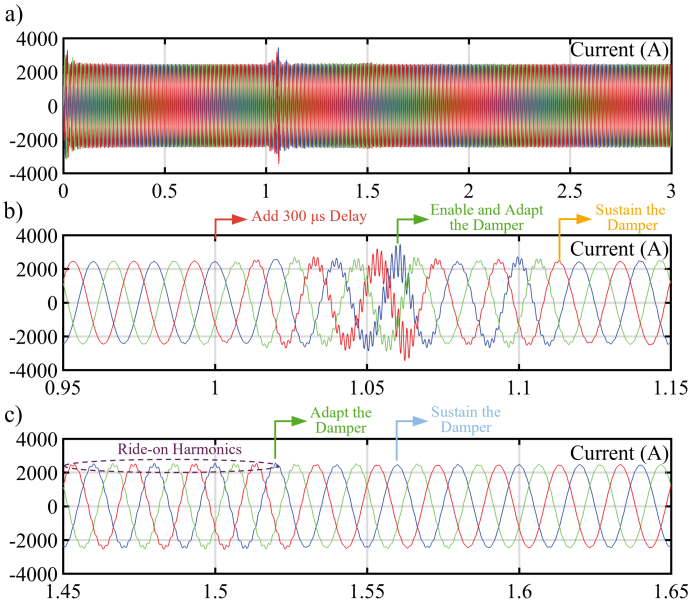

Fig. 9. Simulated time-domain response of MMC: a) overall output current; b) zoom-in view between 0.95 to 1.15 seconds; c) zoom-in view between 1.45 to 1.65 seconds.

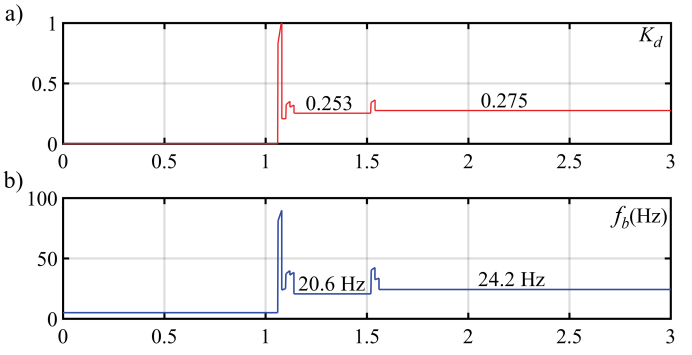

Fig. 10. Adaptive tuning results for: a) K_d; b) f_b of the CCF in the damping function $H_d(s)$.

The simulated MMC current responses are given in Fig. 9, and the aforementioned growing oscillation at 722 Hz appears after the delay is introduced (see Fig. 9 b)). This validates the effectiveness of the lowpass filters designed for current feedback and GVF loop. The growing oscillation is measured by the "Resonance Detection" block within tens of milliseconds and the adaptive narrowband damper is activated, as indicated by the step-up behavior of K_d and f_b shown in Fig. 10. The oscillation is suppressed immediately and the adaptive tuning unit automatically regulates the narrowband damper to a condition where $K_d = 0.253$ and $f_b = 20.6$ Hz at t = 1.14 s. However, one can observe a ride-on oscillation in the MMC current, with its amplitude gradually increasing. At t = 1.56 s, the adaptive tuning unit begins to adjust K_d from 0.253 to 0.275 and f_b from 20.6 Hz to 24.2 Hz. As a result, the slowly-growing harmonic is subsequently mitigated, allowing the MMC to stably transfer power to the grid through OTL.

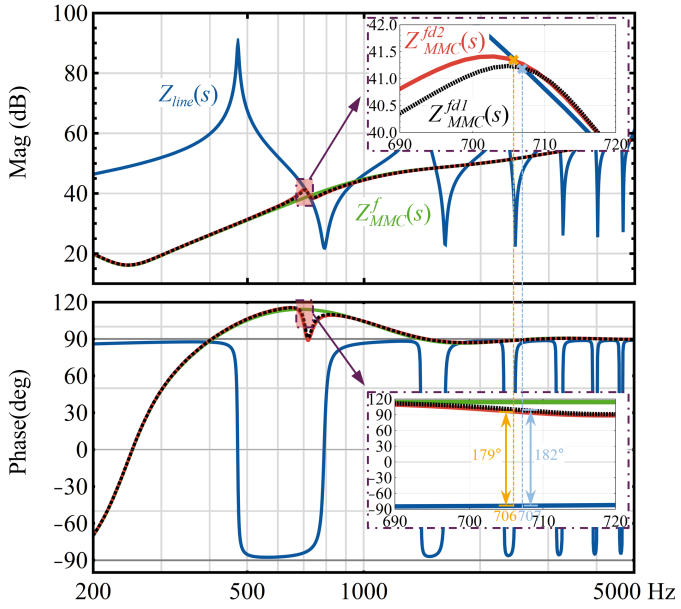

Fig. 11. Impedance responses of: $Z_{line}(s)$, $Z^{f}_{MMC}(s)$, $Z^{fd1}_{MMC}(s)$ and $Z^{fd2}_{MMC}(s)$.

B. Verification by Impedance Responses

To further elucidate the automatic regulation process achieved by the adaptive narrowband damper, the resulting damped impedances of the MMC, labelled as $Z^{fd1}_{MMC}(s)$ and $Z^{fd2}_{MMC}(s)$, are compared with $Z^{f}_{MMC}(s)$ and Z_{line} in Fig. 11. The superscript "*fd1*" denotes Z^{f}_{MMC} damped by Damper 1, with a $K_d = 0.253$ and $f_b = 20.6$ Hz; while the superscript "*fd2*" signifies Z^{f}_{MMC} damped by Damper 2, with a $K_d = 0.275$ and an $f_b = 24.2$ Hz.

As shown in Fig. 11, the inclusion of Damper 1 shifts the magnitude intersection (i.e., resonance frequency) from 722 to 707 Hz, where the phase difference between the MMC and OTL is 182°. This damper quickly suppresses the rapidly growing oscillation at 722 Hz, since the resonance condition at this frequency no longer exists. However, a phase difference of 182° implies the excitation of a new, slowly growing oscillation at 707 Hz. The corresponding effect in time-domain can be seen in Fig. 9 c) between 1.45 to 1.5 seconds, where the ride-on oscillation at 707 Hz is pointed out by dashed-purple circle. When the magnitude of the oscillation at 707 Hz surpasses V_{max} at 1.52 seconds, the adaptive tuning unit adjusts Damper 1 to Damper 2. This adjusted damper reshapes the MMC impedance from $Z^{fd1}_{MMC}(s)$ to $Z^{fd2}_{MMC}(s)$, moving the system resonance to 706 Hz. At 706 Hz, the phase difference between the damped MMC and OTL is less than 180°, effectively eliminating the 722 Hz oscillation without inducing a new oscillation between MMC and OTL.

VI. Conclusion

This paper introduces an adaptive hybrid filtering and damping (AHFD) control method, which combines lowpass filtering and adaptive narrowband damping to mitigate oscillations of the GFL-MMC in the MF/HF range. By using the proposed

design for the AHFD control, the negative damping of the MMC in the HF range is efficiently nullified by lowpass filters, and the stability of control loops remains unaffected. Subsequent to this, the MF oscillation is suppressed using an adaptive narrowband damper that self-adjusts its damping gain and damping range to provide optimal amount of positive damping to the MMC. The EMT simulation results and verification using impedance responses show the effectiveness of the proposed AHFD control scheme.

REFERENCES

[1] P. Huang and L. Vanfretti, "Multi-tuned narrowband damping for suppressing MMC high-frequency oscillations," *IEEE Transactions on Power Delivery*, pp. 1–16, 2023.

[2] H. Saad, Y. Fillion, S. Deschanvres, Y. Vernay, and S. Dennetière, "On resonances and harmonics in HVDC-MMC station connected to ac grid," *IEEE Transactions on Power Delivery*, vol. 32, no. 3, pp. 1565–1573, January 2017.

[3] C. Zou and *et al.*, "Analysis of resonance between a VSC-HVDC converter and the ac grid," *IEEE Transactions on Power Electronics*, vol. 33, no. 12, pp. 10 157–10 168, February 2018.

[4] Y. Li, H. Pang, M. Kong, J. Lu, K. Ji, and G. Tang, "Compensation control and parameters design for high frequency resonance suppression of MMC-HVDC system," *CSEE Journal of Power and Energy Systems*, vol. 7, no. 6, pp. 1161–1175, 2021.

[5] G. Xianshan, Y. Bin, L. Xuan, and Y. Congqi, "Research on the high frequency oscillation of MMC-HVDC integrated into renewable energy system," in *2021 IEEE Southern Power Electronics Conference (SPEC)*, 2021, pp. 1–6.

[6] Z. Xu, B. Li, X. Wang, F. Blaabjerg, and D. Xu, "High-frequency resonance suppression based on unified MMC high-frequency impedance model," *IEEE Transactions on Power Electronics*, vol. 37, no. 12, pp. 14 755–14 769, 2022.

[7] P. Huang and L. Vanfretti, "Adaptive damping control of MMC to suppress high-frequency resonance," *IEEE Transactions on Industry Applications*, pp. 1–14, 2023.

[8] E. Guest, T. W. Rasmussen, and K. H. Jensen, "An impedance-based active filter for harmonic damping by type-IV wind turbine," in *proceedings of 17th Wind Integration Workshop (WIW)*. Energynautics GmbH, 2018, pp. 1–6.

[9] P. Huang and L. Vanfretti, "Adaptive passivity compensation of grid-following MMC for stable grid integration," in *2022 IEEE Industry Applications Society Annual Meeting (IAS)*, 2022, pp. 1–8.

[10] Q. Tu, Z. Xu, and L. Xu, "Reduced switching-frequency modulation and circulating current suppression for modular multilevel converters," *IEEE Transactions on Power Delivery*, vol. 26, no. 3, pp. 2009–2017, 2011.

[11] N. A. Khan, L. Vanfretti, W. Li, and A. Haider, "Hybrid nearest level and open loop control of modular multilevel converters," in *2014 16th European Conference on Power Electronics and Applications*, 2014, pp. 1–12.

[12] H. Wu and X. Wang, "Virtual-flux-based passivation of current control for grid-connected VSCs," *IEEE Transactions on Power Electronics*, vol. 35, no. 12, pp. 12 673–12 677, 2020.

[13] P. Huang and L. Vanfretti, "Analysis of internal energy in GFL-MMCs and a decoupled energy control scheme," in *2023 IEEE Power & Energy Society Innovative Smart Grid Technologies Conference (ISGT)*, 2023, pp. 1–5.

[14] Y. Song, E. Ebrahimzadeh, and F. Blaabjerg, "Analysis of high-frequency resonance in DFIG-based offshore wind farm via long transmission cable," *IEEE Transactions on Energy Conversion*, vol. 33, no. 3, pp. 1036–1046, 2018.

[15] A. Derviškadić, P. Romano, and M. Paolone, "Iterative-interpolated DFT for synchrophasor estimation: A single algorithm for P- and M-class compliant PMUs," *IEEE Transactions on Instrumentation and Measurement*, vol. 67, no. 3, pp. 547–558, 2018.